Purified Mangosteen Peel Extract Mediated-Green Synthesis of Nanostructure Zinc Oxide Incorporated into a Nata de Sago Bacterial Cellulose Transparent Film for UV-Visible Spectroscopy Detection of Hexavalent Chromium in Aqueous Media

Kila Dayana Putri, Abdul Haris Watoni and La Ode Ahmad Nur Ramadhan*
Department of Chemistry, Faculty of Mathematics and Natural Sciences, Halu Oleo University, Kendari, 93231, Indonesia
*Corresponding author (e-mail: laode.ramadhan@uho.ac.id)

This article reports the green synthesis of zinc oxide (ZnO) nanostructures using a purified mangosteen peel extract as a plasmonic dopant in *Nata de Sago* bacterial cellulose transparent films used for the detection of hexavalent chromium (Cr(VI)) in aqueous media by UV-Vis spectroscopy. Purification of the mangosteen extract produced an ethyl acetate-n-hexane fraction and an ethyl acetate-methanol fraction, which act as a reducing agent and capping agent. UV-Vis characterization showed stable ZnO nanostructures with consistent surface plasmon resonance (SPR). FTIR analysis identified -OH, C-H, and Zn-O functional groups, while PSA showed the particle size of ZnO-FEM was smaller (below 100 nm) than ZnO-FEN. SEM and XRD analyses showed that ZnO-FEM had a more dispersed morphology and a smaller crystallite size (8.91–65.92 nm). ZnO-FEM showed superior optical properties with stable fluorescence intensity at an excitation wavelength of 500 nm and a low band gap energy of 1.926 eV. Detection of Cr(VI) by UV-Vis spectrophotometry in the concentration range of 0.01 - 1 ppm using ZnO-FEM 40:50 transparent film showed a good linear relationship (R^2 = 0.9996), good sensitivity with a slope value of 0.6353, good accuracy (102 % recovery) and precision (0.09 % RSD) with an LOD of 0.0138 ppm and LOQ of 0.0188 ppm. The results indicate that the ZnO-FEM 40:50 transparent film has good potential as an optical sensor for Cr(VI) detection by UV-Vis spectrophotometry.

Keywords: Transparent film; *Nata de Sago* bacterial cellulose; zinc oxide; purified mangosteen peel extract; hexavalent chromium

Received: November 2024; Accepted: February 2025

Environmental pollution from heavy metals in industrial waste has become a serious global problem. One of the heavy metals often found in industrial waste is hexavalent chromium (Cr(VI)). Cr(VI) in water and soil is problematic because of its carcinogenic, genotoxic, and mutagenic properties. Cr(VI) exposure can cause various health problems, ranging from skin irritation to respiratory system disorders and organ damage [1]. Therefore, the detection of Cr(VI) in liquid waste before it is discharged into the environment, and the development of such methods, are critical for waste management.

One of the innovations in heavy metal detection methods that is currently the focus of development is the use of environmentally friendly sensor materials. Previously widely applied heavy metal detection methods include inductively coupled plasma-mass spectrometry (ICP-MS) [2] and atomic absorption spectroscopy (AAS) [3]. These methods have good performance but require high costs, sophisticated pretreatment, and professional technicians. To overcome these limitations, transparent films based on bacterial cellulose are designed as a more economical and simple alternative, especially for detecting Cr(VI) metal by UV-Vis spectrophotometry. In this context, *Nata de sago* bacterial cellulose has the potential as a basic matrix for transparent films because it has flexibility, porosity, hydrophilicity, biocompatibility, biodegradability, and is environmentally friendly [4-5]. *Nata de sago* bacterial cellulose can be made through an environmentally friendly process using raw materials from sago liquid waste using *Acetobacter xylinum* bacteria [6]. Thus, *Nata de sago* bacterial cellulose may be used as a sensor matrix incorporating metal oxide nanostructures.

One of the most interesting metal oxides for sensors is zinc oxide (ZnO), due to its properties that support high sensitivity. ZnO nanostructures increase the sensitivity of analyte detection through their surface plasmon resonance (SPR) properties [7]. ZnO is known to have good optical properties, creating great opportunities in sensor applications [8]. ZnO synthesis often uses hazardous chemicals, so this study took a green synthesis approach using mangosteen peel

extracts as an alternative raw material. This plant material contains various bioactive compounds, especially phenolics, such as xanthones, flavonoids, and phenolic acids [9], which can act as reducing agents and capping agents in forming ZnO nanostructures.

Several previous studies have synthesized ZnO using various precursors, such as $Zn(CH_3COO)_2$ [10-16], $ZnCl_2$ [17], ($Zn(NO_3)_2$ [18-19], $Zn(C_{17}H_{33}COO)_2$ [20], and green synthesis using rambutan peel extract (*Nephelium lappaceum* L.) [21], banana peel extract [22], *Salvia officinalis* leaf extract [23], pineapple peel extract [24], loquat seed extract [25], and rosemary extract [26]. The purification process of the mangosteen peel extract aimed to improve the quality of ZnO nanostructures with better optical properties and stability. Isolation of active compounds for ZnO synthesis is rarely attempted. In addition, the utilization of certain fractions of mangosteen peel extract, especially the polar and non-polar fractions of the purified extract, has not been widely studied. These fractions are expected to increase the interactions and sensitivity of ZnO in detecting Cr(VI).

The novelty of this study is the development of a transparent film based on *Nata de Sago* bacterial cellulose incorporated with ZnO nanostructure-purified mangosteen peel extract for Cr(VI) detection using a UV-Vis spectrophotometer in aqueous media. The innovation lies in the utilization of environmentally friendly materials, namely *Nata de Sago* bacterial cellulose, which functions as a transparent film matrix, ZnO synthesized with the help of a natural capping agent from mangosteen peel, and extract purification using the ethyl acetate-n-hexane and ethyl acetate-methanol fractions which have not been widely explored in heavy metal sensor applications. The resulting transparent film had a unique ability to respond to UV light with changes in optical characteristics sensitive to variations in Cr(VI) concentration. This study focused on two main aspects, namely the characterization of the transparent film of *Nata de Sago* bacterial cellulose incorporated with ZnO nanostructure-purified mangosteen peel extract, and the validity of the film as an efficient optical sensor in detecting Cr(VI). With this approach, it is hoped that a more economical, portable, and environmentally friendly detection method will be created with significant sensitivity and low detection limits.

EXPERIMENTAL

Chemicals and Materials

The materials used in this study were mangosteen peel waste, sago liquid waste, granulated sugar (Gulaku), ammonium sulfate or *zwavelzure ammoniac* (ZA), acetic acid (Emsure Merck), *Acetobacter xylinum* bacterial starter, Whatman No. 42 filter paper, 96 % ethanol (Emsure Merck), silica gel 60, n-hexane (Emsure Merck), ethyl acetate (Emsure Merck), methanol (Emsure Merck), $Zn(NO_3)_2.4H_2O$ (Emsure Merck), sodium hydroxide (NaOH) (Emsure Merck), potassium dichromate (Emsure Merck), distilled water (Water One), and epoxy resin.

The tools used in this study were a pH meter (Mettler Toledo), hydrothermal autoclave reactor, 4000 RPM 220V centrifuge (Laborglas), oven, rotary evaporator (Buchi), vacuum column chromatograph (KKV), furnace, hotplate stirrer, handpress, laminar air flow, gas chromatography-mass spectroscopy instrument (Shimadzu), UV-Vis spectrophotometer (Vernier), fluorescence spectrometer (Vernier), FTIR spectrophotometer (Shimadzu), particle size analyzer (Beckman Coulter), scanning electron microscope (JEOL JSM-6360), and X-ray diffractometer (PANalytical).

Synthesis and Characterization Methods

Preparation and Purification of Mangosteen Peel Extract

The mangosteen peel extraction method was adapted from the procedure described by Fadhila et al. (2022) [27]. Mangosteen fruits were washed, and the peels were separated from the flesh, thinly sliced, dried, and ground into powder. A total of 500 g of the powder was macerated with 2000 mL of 96 % ethanol for 72 hours. The mixture was then filtered, and the filtrate was evaporated at 50 °C using a rotary evaporator. The extract was purified using vacuum liquid chromatography (VLC) with silica gel as the stationary phase [28], and a mixture of n-hexane:ethyl acetate solvent as the mobile phase, with volume ratios of 9:1, 8:2, 5:5, followed by ethyl acetate 100 %, and methanol. The resulting fractions were analyzed using GC-MS to identify the active components [29], and to obtain a purified extract.

Green Synthesis of Zinc Oxide Nanostructure-Purified Mangosteen Peel Extract

Zinc oxide (ZnO) was synthesized by a green chemistry technique, with purified mangosteen peel extract as a capping agent. Six beakers were each filled with 50 mL of 0.02 M $Zn(NO_3)_2 \cdot 4H_2O$, to which were added 5, 10, 20, 30, 40, and 50 mL of mangosteen peel extract from the ethyl acetate-n-hexane fraction and ethyl acetate-methanol fraction. This resulted in samples of ZnO-mangosteen peel extract in the ethyl acetate-n-hexane fraction in the following ratios: ZnO-FEN 5:50, ZnO-FEN 10:50, ZnO-FEN 20:50, ZnO-FEN 30:50, ZnO-FEN 40:50, and ZnO-FEN 50:50, as well as samples of ZnO-mangosteen peel extract in the ethyl acetate-methanol fraction in the following ratios: ZnO-FEM 5:50, ZnO-FEM 10:50, ZnO-FEM 20:50, ZnO-FEM 30:50, ZnO-FEM 40:50, and ZnO-FEM 50:50. Each mixture was stirred using a magnetic stirrer at 70 °C for 1 hour, and 0.45

M NaOH solution was slowly added until the pH reached 12. The mixture was then left overnight and then centrifuged to form a stable precipitate. The resulting precipitate was washed carefully with distilled water. The washed precipitate was annealed in a hydrothermal autoclave reactor at 100 °C, followed by calcination at 450 °C for 4 hours to obtain ZnO nanostructures.

Synthesis of *Nata de Sago* Bacterial Cellulose

The sago liquid waste was filtered and transferred into a clean container. The synthesis method followed the procedure by Yanti et al. (2023) [30] as follows: 450 g of granulated sugar and 45 g of ammonium sulfate (*zwavelzure ammoniak*/ZA) were added to 3000 mL of sago liquid waste, and heated until boiling. After cooling, 30 mL of 25 % acetic acid and 750 mL of *Acetobacter xylinum* were added, stirred slowly, and poured into a sterilized container. The mixture was covered with newspaper and fermented for 10 days until a thin layer of *Nata* was formed.

Synthesis of a Transparent Film of *Nata de Sago* Bacterial Cellulose Incorporated with Nanostructured Zinc Oxide-Purified Mangosteen Peel Extract

The fermented *Nata de sago* bacterial cellulose was washed with distilled water and soaked in 2 % NaOH solution for 5 minutes, then rinsed with running water until a neutral pH was achieved. The *Nata de sago* bacterial cellulose was pressed using a hand press to produce thin film sheets. The film was cut into pieces measuring 4 × 0.8 cm, soaked in an epoxy resin mixture, and dried for 24 hours to produce a transparent and sturdy film. The film was then immersed in a solution of the ZnO nanostructure-purified mangosteen peel extract until a colour change occurred.

Film Test

Spectroscopic film testing used chromium metal analyte samples that interacted with the transparent *Nata de sago* bacterial cellulose films incorporated with the ZnO nanostructure-purified mangosteen peel extract. The film was used as an optical sensor in UV-Vis spectroscopy to measure the absorbance of standard Cr(VI) solutions at concentrations of 0.01, 0.04, 0.07, 0.10, 0.40, 0.70, and 1.00 ppm at a maximum wavelength of 392 nm. The resulting linear graph was used as a calibration curve to determine the Cr(VI) concentration in nickel smelter wastewater samples. After establishing the concentration range for the calibration curve, method validation was performed to determine the LOD (Limit of Detection), LOQ (Limit of Quantification), sensitivity, accuracy, and precision, and to measure Cr(VI) concentrations in wastewater samples.

Characterization

The characterisation analyses carried out included stability analysis of the purified ZnO-mangosteen peel extract using UV–visible spectroscopy, fluorescence analysis using a fluorescence spectrophotometer, functional group analysis using Fourier Transform infrared spectroscopy (FTIR), particle size analysis using a particle size analyzer (PSA), morphology analysis using a scanning electron microscope (SEM), and crystal structure analysis using X-ray diffraction (XRD).

RESULTS AND DISCUSSION

Extract and Purification of Mangosteen Peel Extract

Extraction of 250 g of powdered mangosteen peel by maceration with 96 % ethanol produced 18 g of thick extract with a yield of 7.2 %. Purification of the extract using vacuum liquid chromatography (VLC) produced 2 fractions, an ethyl acetate-n-hexane fraction and an ethyl acetate-methanol fraction (Figure 1). The ethyl acetate-n-hexane fraction was yellow while the ethyl acetate-methanol fraction was brownish yellow.

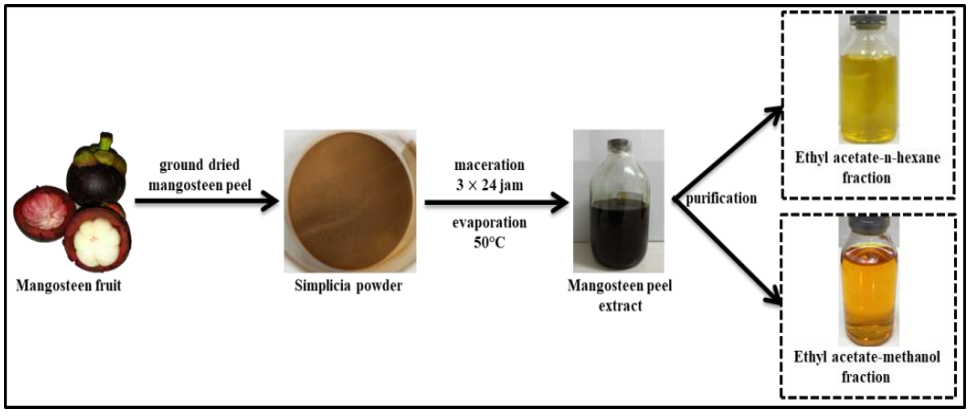

Figure 1. Purification scheme for the mangosteen peel extract.

The GC-MS analysis results of the ethyl acetate-n-hexane fraction are presented in Table 1. These compounds have potential as capping agents in the synthesis of ZnO nanostructures because they are thought to affect the stability, size, and shape of the resulting ZnO nanostructures. The chemical properties of the compounds in this fraction should contribute optimally to controlling particle growth during the synthesis process.

Meanwhile, the GC-MS analysis results for the ethyl acetate-methanol fraction revealed a different phytochemical composition (Table 2). These components have potential roles in the synthesis process because they affect the surface properties and morphology of ZnO nanostructures differently compared to the ethyl acetate-n-hexane fraction.

The green synthesis mechanism of plant-based ZnO involves the use of phytochemicals in plant extracts as reducing and stabilizing agents (Figure 2). Phytochemicals present in both fractions of the purified mangosteen peel extract, such as 9-octadecenal, oleic aldehyde, methyldiethylborane, squalene diepoxide, 12-tricosanone, octadecanoic acid, 16-hentriacontanone, and dodecanoic acid, influence the nanostructure synthesis process, with factors such as pH and temperature playing crucial roles. In the study by Sun et al., 2023, it was explained that metals like copper, silver, gold, titanium, zinc, iron, and nickel can form metal oxides through phytochemical activity to produce metal oxide nanostructures. This phenomenon is highly relevant to plant-based ZnO synthesis, where phytochemicals in plant extracts serve not only as reducing agents but also as capping agents for the formed ZnO nanoparticles [31]. However, it is important to further analyze how the phytochemical compounds used may affect the morphology and photocatalytic properties of the resulting metal oxide nanostructures, as the influence of various phytochemicals on synthesis and stability is not yet fully understood. Therefore, in plant-based ZnO synthesis, phytochemicals in specific plant extracts can play a role in controlling not only the reduction of metal ions to ZnO but also in influencing its photocatalytic properties. Further research is needed to explore the interactions between phytochemical compounds and Zn^{2+} ions under various synthesis conditions, as well as how these factors may affect the structural and photocatalytic properties of the resulting ZnO.

Table 1. GC-MS analysis of ethyl acetate-n-hexane fraction.

R. Time	Area	Area %	Molecular Structure	Compound
14.943	811620	8.88	$C_{18}H_{34}O$	9-Octadecenal
15.739	1164565	12.74	$C_{18}H_{34}O$	Epoxycyclododecane
26.461	1190818	13.03	$C_5H_{13}B$	Methyldiethylborane
28.283	1521218	16.64	$C_{30}H_{52}O_2$	Squalene diepoxide

Table 2. GC-MS analysis of the ethyl acetate-methanol fraction.

R. Time	Area	Area %	Molecular Structure	Compound
22.298	4793459	3.51	$C_{23}H_{46}O$	12-Tricosanone
23.668	5293138	3.88	$C_{20}H_{38}O_2$	Octadecanoic acid
25.017	5163046	3.78	$C_{31}H_{62}O$	16-Hentriacontanone
26.485	15228246	11.16	$C_5H_{13}B$	Methyldiethylborane
28.295	17125611	12.55	$C_{18}H_{34}O$	9-Octadecenal
29.821	10536722	7.72	$C_{39}H_{74}O_6$	Dodecanoic acid

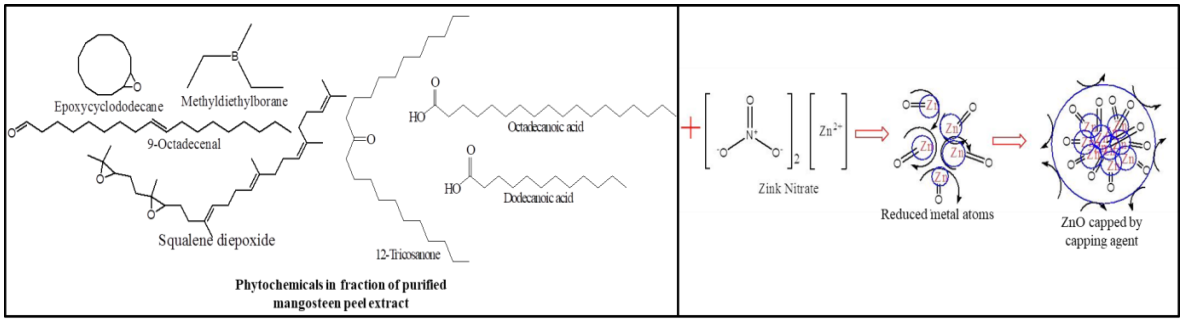

Figure 2. Green synthesis mechanism of ZnO nanostructures.

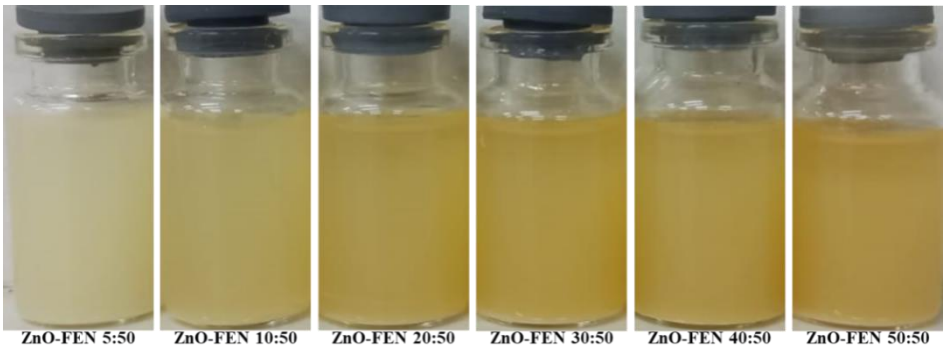

Figure 3. ZnO-ethyl acetate-n-hexane fraction of the purified mangosteen peel extract.

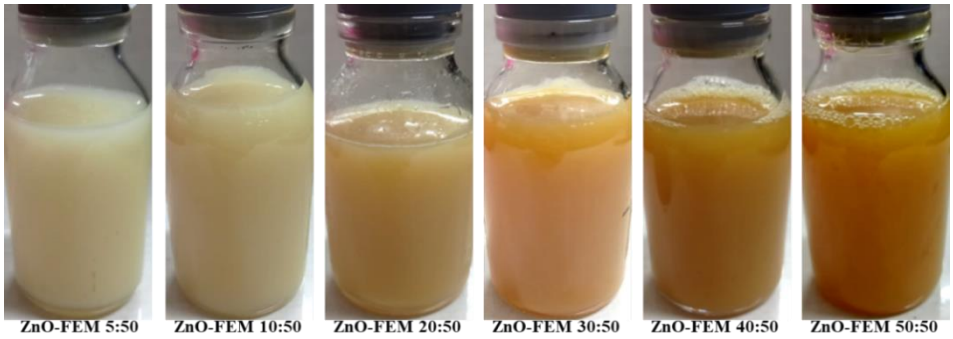

Figure 4. ZnO-ethyl acetate-methanol fraction of the purified mangosteen peel extract.

Green Synthesis of Zinc Oxide with Purified Mangosteen Peel Extract

Stability Analysis using UV–visible spectroscopy

Green synthesis of ZnO using mangosteen peel extract is an environmentally friendly method that utilizes natural components as reducing agents and capping agents. This synthesis involves both the ethyl acetate-n-hexane and ethyl acetate-methanol fractions of the purified mangosteen peel extract, where the capping agent plays a role in controlling the size and shape of ZnO. Variations in the volume ratio used in ZnO synthesis allow research on the effect of the amount of capping agent on the size and morphology of the ZnO formed. The addition of NaOH until the solution reaches pH 12 creates the strong basic conditions needed to precipitate $Zn(OH)_2$. The ZnO-ethyl acetate-n-hexane fraction of the purified mangosteen peel extract can be seen in Figure 3, and the ZnO-ethyl acetate-methanol fraction can be seen in Figure 4.

After synthesis, the obtained precipitate was centrifuged to separate ZnO from the solution. A washing process with distilled water was carried out to neutralize the pH of the precipitate. Annealing in a hydrothermal container in an oven with a controlled temperature of 100 ºC helped to remove moisture before calcination. Calcination at 450 ºC for 4 hours was required to completely convert $Zn(OH)_2$ to ZnO and to increase the crystallinity of the ZnO nanostructure. The ZnO powder-ethyl acetate-n-hexane fraction is shown in Figure 5, while the ZnO powder-ethyl acetate-methanol fraction is shown in Figure 6. The ZnO powder obtained from both fractions exhibited a white to slightly yellowish-white appearance, consistent with the findings of previous studies [32].

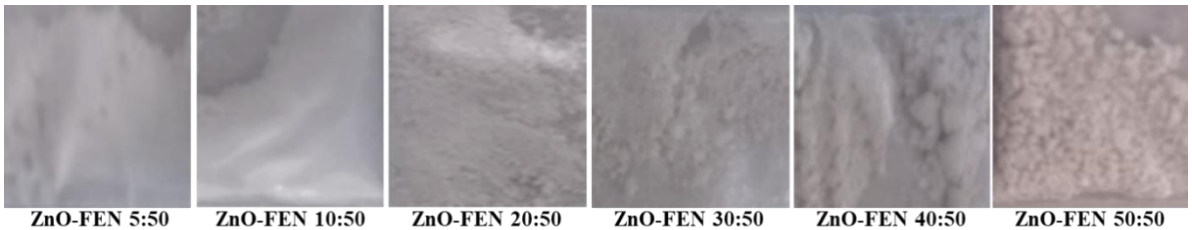

Figure 5. ZnO powder-ethyl acetate-n-hexane fraction.

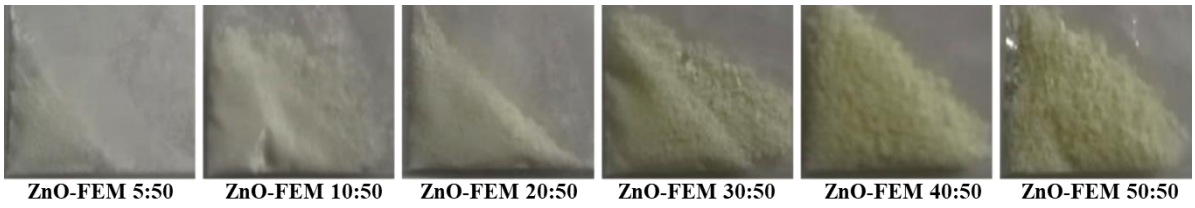

Figure 6. ZnO powder-ethyl acetate-methanol fraction.

Stability Analysis using UV–visible Spectroscopy

The UV-Vis spectra show the difference in absorption between ZnO-FEN (ethyl acetate-n-hexane fraction) and ZnO-FEM (ethyl acetate-methanol fraction), which is influenced by the capping agent used. The ZnO-FEN spectrum had a smaller and non-uniform variation in absorption intensity, with the highest peak in the ZnO-FEN 50:50 fraction around the wavelength of 400 nm, while the ZnO-FEM spectrum showed a greater absorption intensity and a more uniform absorption pattern throughout the fraction. This was possible due to different interactions between ZnO and the two fractions. The shift in the absorption wavelength also reflects the differences in the optical properties of the mixture caused by the type of fraction used.

The stability of the purified ZnO-mangosteen peel extract can be observed through the Surface Plasmon Resonance (SPR) absorption peak within a time span of 30 minutes. In this study, the SPR absorption peaks in both ZnO-FEN (ethyl acetate-n-hexane fraction) and ZnO-FEM (ethyl acetate-methanol fraction) remained consistent without significant change for 30 minutes. This indicates that the ZnO in both fractions had good stability. The formation of ZnO nanostructures was not only marked by changes in the colour of the solution, but also by the presence of absorption peaks at certain wavelength ranges, usually in the range of 200-600 nm [33]. This consistency indicates that the successfully synthesized ZnO nanostructures had optimum stability. The UV-Vis absorption spectra of the ethyl acetate-n-hexane fraction and ZnO-ethyl acetate-n-hexane fraction of the purified mangosteen peel extract are shown in Figure 7. The UV-Vis absorption spectra of the ethyl acetate-methanol fraction and ZnO-ethyl acetate-methanol fraction of the purified mangosteen peel extract are displayed in Figure 8.

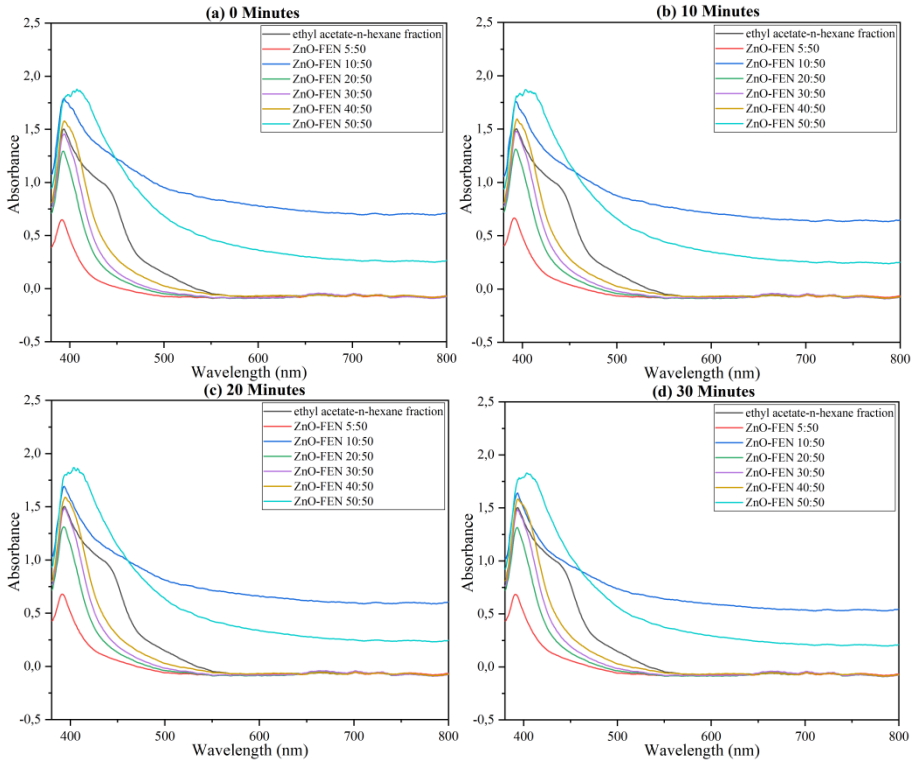

Figure 7. UV-Vis absorption spectra of the ethyl acetate-n-hexane fraction and ZnO-ethyl acetate-n-hexane fraction of the purified mangosteen peel extract.

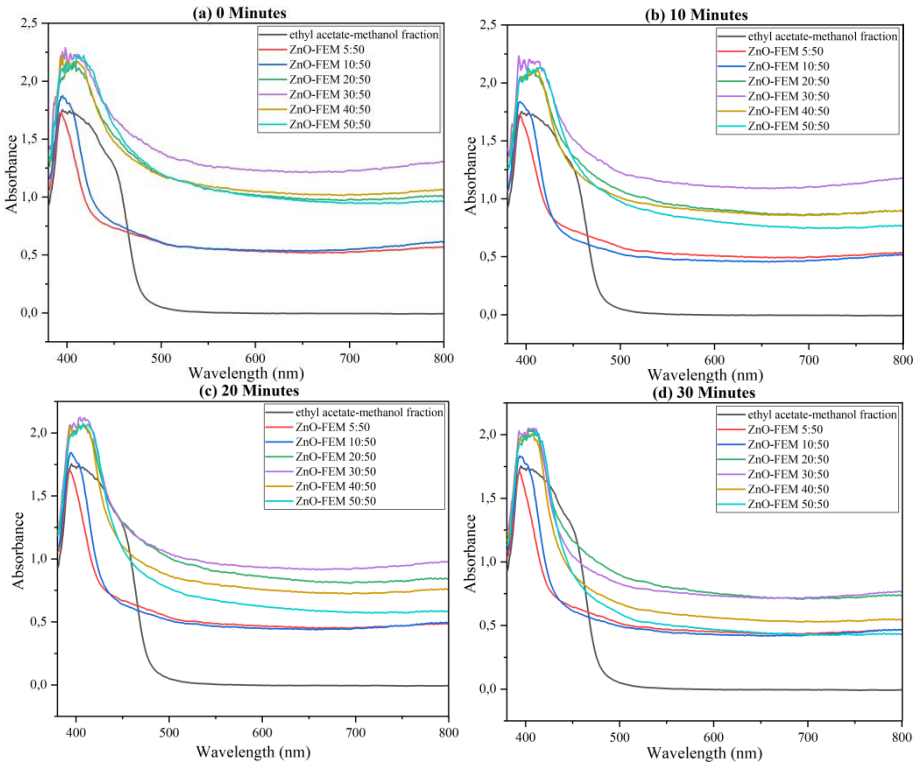

Figure 8. UV-Vis absorption spectra of the ethyl acetate-methanol fraction and ZnO-ethyl acetate-methanol fraction of the purified mangosteen peel extract.

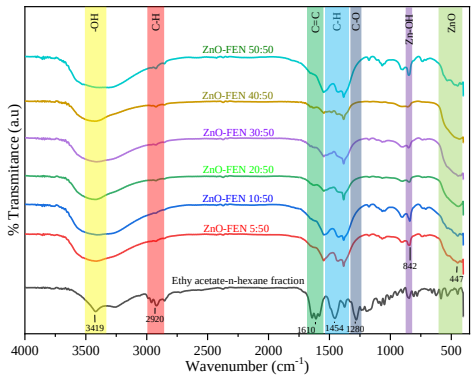

Figure 9. FTIR spectra of ZnO-ethyl acetate-n-hexane fraction.

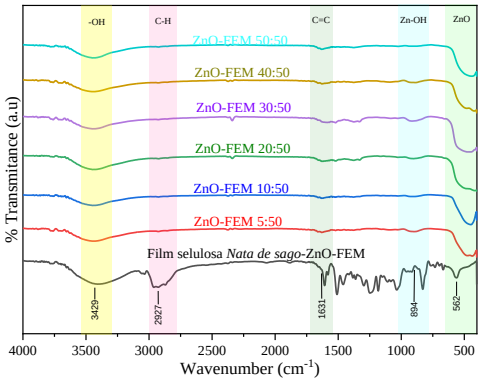

Figure 10. FTIR spectra of transparent films of *Nata de sago* bacterial cellulose-ZnO-ethyl acetate-methanol fraction and ZnO-ethyl acetate-methanol fraction.

Functional Group Analysis Using Fourier Transform Infrared (FTIR)

FTIR analysis was carried out to identify the functional groups in the ZnO-ethyl acetate-n-hexane and ZnO-ethyl acetate-methanol fractions.

As seen in Figure 9, the FTIR spectrum for the ZnO-ethyl acetate-n-hexane fraction showed energy bands at 3419 cm^{-1}, 2920 cm^{-1}, 1610 cm^{-1}, 1454 cm^{-1}, 1280 cm^{-1}, 842 cm^{-1}, and 447 cm^{-1}, which indicated -OH, stretching C-H, C=C, bending C-H, C-O, Zn-OH, and Zn-O groups, respectively. The peak at 3419 cm^{-1} indicated the presence of hydroxyl groups (-OH) which can come from moisture or hydroxyl groups bound to the surface of the ZnO material. The peak at 2920 cm^{-1}, characteristic of aliphatic C-H vibrations, implied that the material contained organic components, which were likely derived from polymer compounds or surfactants bound to ZnO. The presence of a peak at 1454 cm^{-1} was consistent with C-H bending, and confirmed the presence of hydrocarbon compounds in the sample structure. Meanwhile, the absorption at 1280 cm^{-1}, associated with C-O vibrations, implied the presence of ether or alcohol groups in the sample. Furthermore, there was an absorption band at 840 cm^{-1}, characteristic of Zn-OH vibrations. This band indicated the interaction of H_2O molecules on the surface of ZnO nanostructures which may be caused by physical or chemical absorption of water on the surface of the material. Thus the ZnO surface of the sample may be hydrophilic, which allows for the adsorption of water molecules. In addition, a sharp peak at 447 cm^{-1}, identified as the stretching vibration of Zn-O bonds, is an indication of the presence of ZnO.

The FTIR spectrum for the ZnO-ethyl acetate-methanol fraction in Figure 10 showed a similar absorption pattern to the ZnO-ethyl acetate-n-hexane fraction, where the peaks at 3429 cm^{-1}, 2927 cm^{-1}, 1631 cm^{-1}, 894 cm^{-1}, and 562 cm^{-1} indicated the presence of –OH, C-H, C=C, Zn-OH, and Zn-O groups, respectively. However, variations in the intensity of some peaks indicated differences in structure and composition between the two samples. The shift in wave numbers around 500 cm^{-1} was suspected to be due to van der Waals interactions between ZnO-FEM and the *Nata de sago* bacterial cellulose transparent film matrix.

The FTIR spectra showed that both the ZnO-ethyl acetate-n-hexane and ZnO-ethyl acetate-methanol fractions contained hydroxyl groups, organic compounds, and ZnO, but the difference in peak intensities between the two indicated variations in concentration and molecular interactions in their respective structures. The volume ratio greatly affected the interaction of functional groups with the ZnO nanostructures. These peaks were consistent with the characteristics of functional groups that are often found in ZnO nanostructures with bioactive compounds from mangosteen peel extract as capping agents. ZnO is one of the metal oxides with characteristic peaks in the range of 400-900 cm^{-1} [34].

Particle Size Analysis Using a Particle Size Analyzer (PSA)

Analysis using PSA was carried out to determine the particle size of the ZnO-ethyl acetate-n-hexane and ZnO-ethyl acetate-methanol fractions. The PSA results of the ZnO-ethyl acetate-n-hexane fraction showed variations in the average particle size at the ZnO comparison ratio, with ZnO-FEN 10:50, ZnO-FEN 20:50, ZnO-FEN 30:50, and ZnO-FEN 40:50 giving average particle sizes of 329.52 nm, 350.86 nm, 505.50 nm, and 260.6 nm, respectively (Figure 11). The average particle size for both ZnO-FEN 5:50 and ZnO-FEN 50:50 was likely to be above 3500 micrometers. Due to the detection limits of the instrument, it was unable to analyze particles that were too large due to agglomeration occurring in the nanoparticle formation process.

The PSA results of the ZnO-ethyl acetate-methanol fraction samples showed a significant variation in the average particle size at various ZnO ratios, with ZnO-FEM 5:50, ZnO-FEM 10:50, ZnO-FEM 20:50, ZnO-FEM 30:50, ZnO-FEM 40:50, and ZnO-FEM 50:50, giving particle sizes of 60.92 nm, 67.69 nm, 73.55 nm, 445.01 nm, 50.49 nm, and 70.66 nm, respectively (Figure 12). From these results, it can be seen that the particle size gradually increased from ZnO-FEM 5:50 to ZnO-FEM 20:50; this could be caused by the growth of larger particles due to changes in synthesis conditions or the composition of the ethyl acetate-methanol fraction. However, in ZnO-FEM 30:50, there was a drastic increase in particle size to 445.01 nm which is likely to be due to agglomeration.

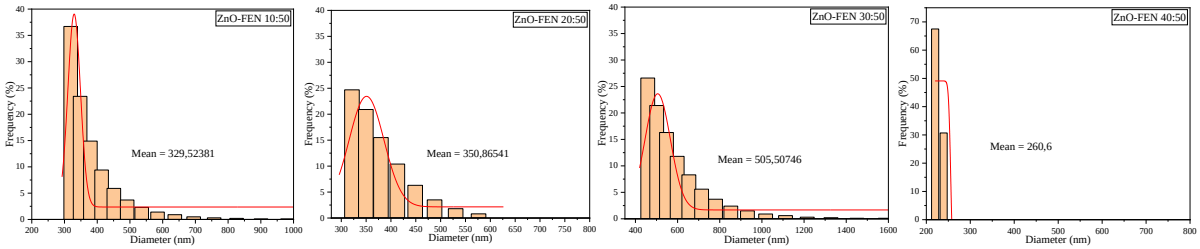

Figure 11. PSA results for the ZnO-ethyl acetate-n-hexane fraction.

Agglomeration of ZnO particles and non-uniformity of particle sizes occur due to the influence of solvent polarity, electrostatic power, and high surface energy. During the synthesis process, ZnO particles tend to stick together because the solvent polarity is not stable enough to keep the particles separate, especially if the solvent cannot withstand the attractive force between particles. In addition, ZnO particles have a surface charge that can cause attractive forces between particles if the repulsive force is not strong enough. The high surface energy of ZnO particles also encourages agglomeration, because small particles tend to combine to reduce the surface free energy [35].

Green synthesis of ZnO in the ethyl acetate-methanol fraction produced ZnO particles with an average size smaller than 100 nm, compared to the ethyl acetate-n-hexane fraction which tended to produce particles with sizes above 200 nm. This shows that the ethyl acetate-methanol fraction was more effective in preventing agglomeration and producing smaller-sized particles.

Scanning Electron Microscope (SEM) Morphological Analysis

SEM analysis showed that the ZnO-mangosteen peel extract was purified in the ethyl acetate-n-hexane fraction of the synthesis product using precursor-mangosteen peel extract, with varying precursor: extract volume ratios producing different morphologies (Figure 13).

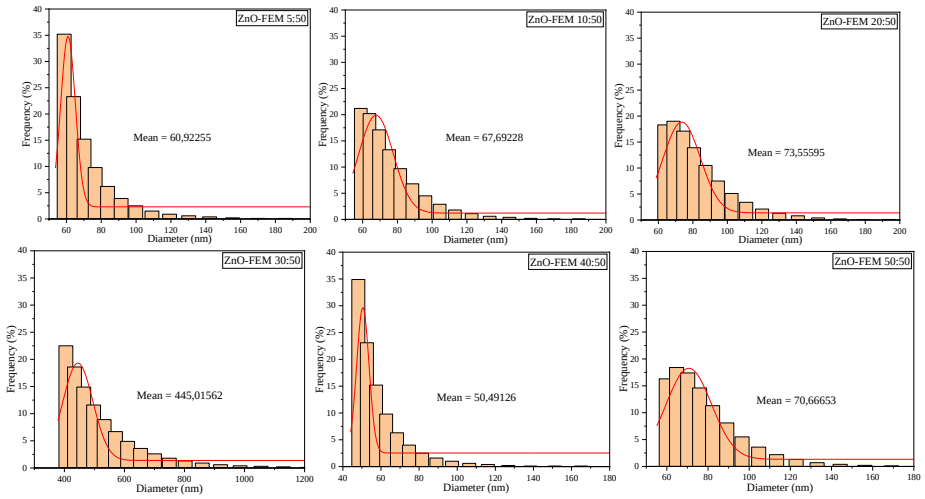

Figure 12. PSA results for the ZnO-ethyl acetate-methanol fraction.

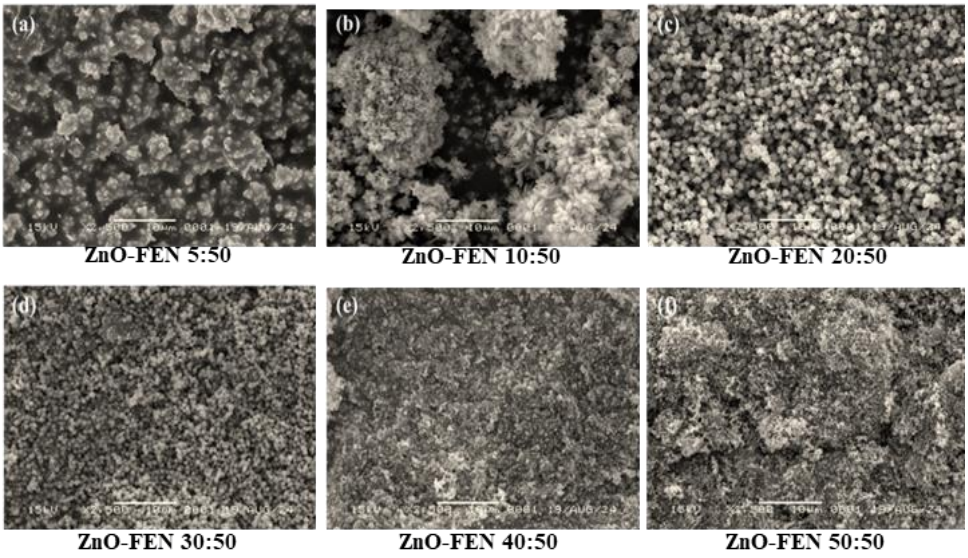

Figure 13. SEM images of the ZnO powder-ethyl acetate-n-hexane fraction of the purified mangosteen peel extract at 2500x magnification.

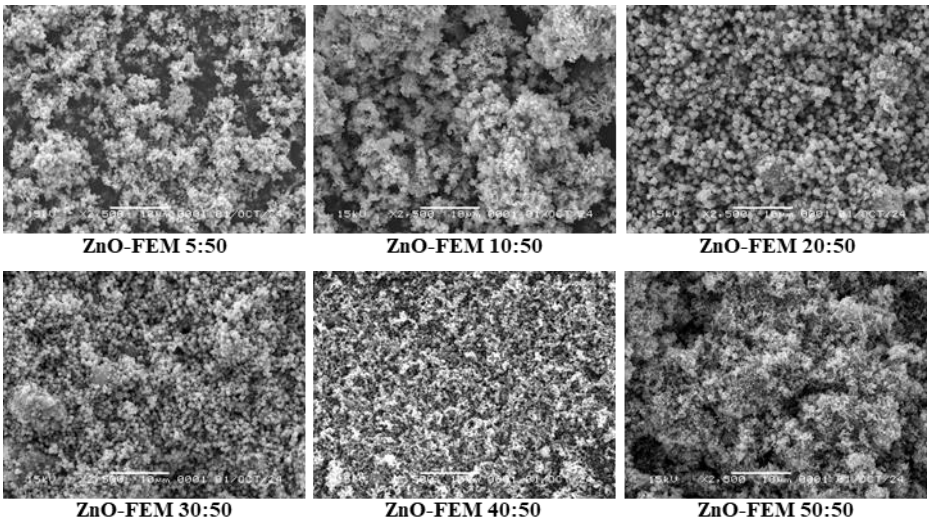

Figure 14. SEM images of ZnO powder-ethyl acetate-n-methanol fraction of the purified mangosteen peel extract at 2500x magnification.

The ZnO-FEN 20:50 and ZnO-FEN 30:50 particles were evenly distributed, while the other particles showed agglomeration. The particles in ZnO-FEN 5:50 appeared to be granular or grainy aggregates. This structure showed small particles that appeared to stick to each other, possibly forming agglomerations. This form is often seen in nanoparticles that tend to gather together due to interparticle forces. In ZnO-FEN 10:50, the particles appeared to have flower-like structures, showing a more complex shape with particle aggregation forming large groups. This form is often referred to as the ZnO flower structure, where small particles gather to form larger structures and resemble flower petals. The particles in ZnO-FEN 20:50 appeared more spherical or round and more dispersed than the other images. This indicates particles with a more regular and uniform morphology, which confirms previous research [36].

The particles of ZnO-FEN 30:50 appeared relatively uniform and fine-grained, forming a dense structure. The particles were close together but not completely merged, indicating fairly good particle dispersion without major agglomeration. In ZnO-FEN 40:50, the particles appeared more compact with a rough surface, indicating further aggregation compared to ZnO-FEN 30:50. This structure may indicate particles adhering to each other, forming a denser agglomeration structure. The particles in ZnO-FEN 50:50 had a larger and more irregular structure, with significant clumping. This indicates severe agglomeration, where small particles gather to form large, unevenly dispersed clusters.

The SEM images of the ZnO powder-ethyl acetate-methanol fraction of the purified mangosteen peel extract are shown in Figure 14. The particles of ZnO-FEM 5:50, ZnO-FEM 10:50, ZnO-FEM 20:50, ZnO-FEM 30:50, ZnO-FEM 40:50, and ZnO-FEM 50:50 appeared well dispersed and formed finer and more uniform structures compared to those of the ZnO-ethyl acetate-n-hexane fraction. This indicates that the ethyl acetate-methanol fraction was more effective in reducing agglomeration and maintaining small particle size. The morphology of the ZnO-FEM 5:50 particles showed nano sizes with little agglomeration. In ZnO-FEM 10:50, larger and aggregated particles were seen, forming a flower-like structure. This indicates a more complex particle growth. Despite agglomeration, the particles retained their unique nanostructures. The ZnO-FEM 20:50 particles appeared denser compared to the other images, indicating a more uniform dispersion due to agglomeration. These particles appeared more regular and spherical in shape. In ZnO-FEM 30:50, the particles appeared irregular in shape and showed agglomeration, where many small particles combine to form a coarse structure. In contrast, ZnO-FEM 40:50 exhibited finer and more evenly distributed particles, with a more uniform size and less agglomeration. The surface structure of this sample appeared denser and more compact. However, the particles in ZnO-FEM 50:50 appeared larger, uneven and tended to clump.

Crystal Structure Analysis by X-Ray Diffraction (XRD)

The X-ray diffraction results of the ZnO-ethyl acetate-n-hexane fraction are shown in Figure 15 while those of the ZnO-ethyl acetate-methanol fraction are shown in Figure 16. The ZnO-ethyl acetate-n-hexane and ZnO-ethyl acetate-methanol fractions had relatively similar diffraction patterns, with scattering angles (2θ) of 31.79º, 34.45º, 36.26º, 47.54º and 56.59º corresponding to the lattice planes (100), (002), (101), (102) and (110) based on JCPDS No. 00-001-1136 data. These observations confirm that the ZnO-ethyl acetate-n-hexane fraction exhibited a hexagonal wurtzite structure [37].

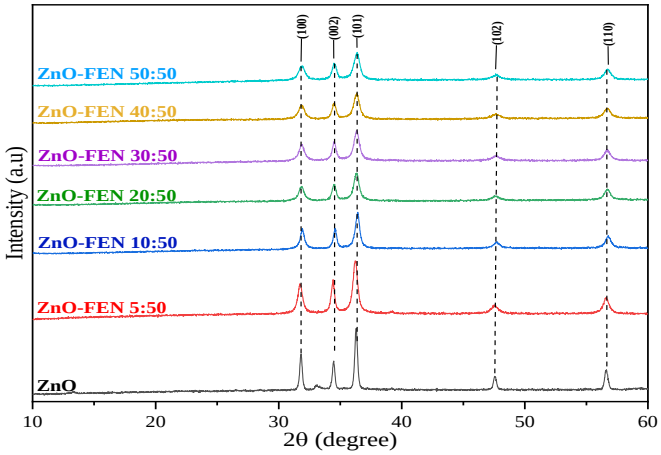

Figure 15. XRD diffraction pattern of the ZnO-ethyl acetate-n-hexane fraction.

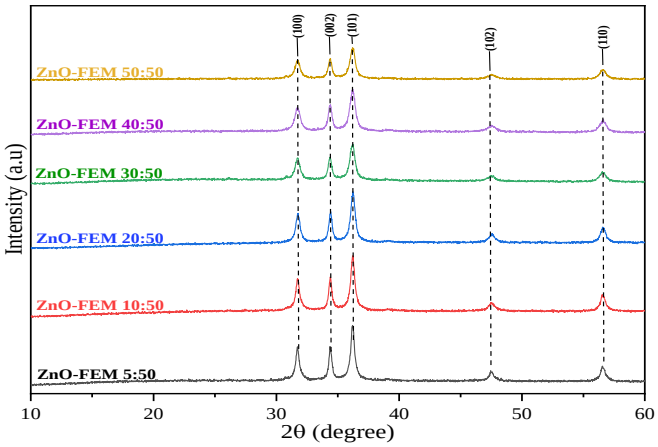

Figure 16. XRD diffraction pattern of the ZnO-ethyl acetate-methanol fraction.

The crystallite sizes of the synthesised ZnO-ethyl acetate-n-hexane and ZnO-ethyl acetate-methanol fractions were calculated using the Debye Scherrer equation:

$$D = \frac{k \times \lambda}{\beta \cos \theta}$$

where D is the crystallite size (nm), k is a constant of 0.9, λ is the wavelength of X-ray radiation (0.154 nm), β is the FWHM, and θ is the Bragg angle. Based on this calculation, the crystallite sizes of ZnO-FEN 5:50, ZnO-FEN 10:50, ZnO-FEN 20:50, ZnO-FEN 30:50, ZnO-FEN 40:50 and ZnO-FEN 50:50 were 65.92, 57.02, 28.83, 40.03, 30.97 and 39.15 nm, respectively. For ZnO-FEM 5:50, ZnO-FEM 10:50, ZnO-FEM 20:50, ZnO-FEM 30:50, ZnO-FEM 40:50, and ZnO-FEM 50:50, the crystallite sizes obtained were 11.59, 11.97, 10.11, 9.78, 9.60 and 8.91 nm, respectively. These results indicate that variations in the ratio of ZnO-FEN and ZnO-FEM significantly affected the resulting crystallite size. This finding is a new contribution to the development of ZnO materials, especially as the results of these calculations differ from those reported in previous studies [38], [39], [40], which generally showed larger or smaller crystallite sizes without such a striking effect caused by the ratio.

Nata de Sago Bacterial Cellulose

The *Nata de sago* bacterial cellulose was fermented for 10 days. The *Nata* layer formed was slightly translucent white and had a chewy texture (Figure 17). This finding confirms the results of previous studies that showed similar characteristics in the *Nata* fermentation process [41]. Fermentation of 1000 mL of sago liquid waste produced around 957 g of wet *Nata* (yield = 95.75 %).

Figure 17. *Nata de sago* bacterial cellulose from fermentation.

Figure 18. Transparent film of *Nata de sago* bacterial cellulose-ZnO-ethyl acetate-methanol fraction.

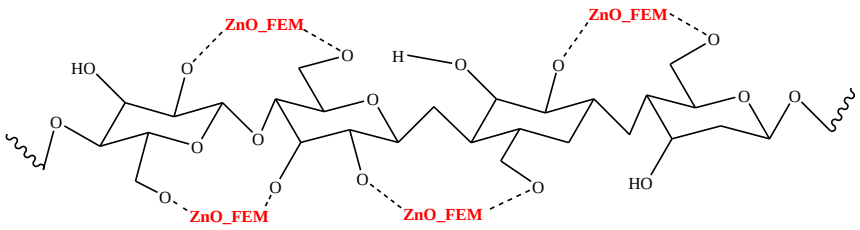

Figure 19. Proposed interaction of bacterial cellulose with the ZnO-purified mangosteen peel extract of the ethyl acetate-methanol fraction.

Transparent Film Incorporated with Zinc Oxide-Purified Mangosteen Peel Extract

The ZnO-ethyl acetate-methanol fraction was chosen as the plasmonic dopant in the synthesis of UV-Vis spectrophotometric sensor films because its particle size was in the nanometre scale. In this study, a *Nata de sago* bacterial cellulose-ZnO-purified mangosteen peel extract composite of the ethyl acetate-methanol fraction was obtained by soaking the *Nata de sago* bacterial cellulose film in a ZnO-ethyl acetate-methanol fraction suspension. Figure 18 shows a transparent film of *Nata de sago* bacterial cellulose combined with ZnO-ethyl acetate-methanol fraction. This film had a transparent appearance and was in the form of a thin sheet, with a slightly translucent white colour.

The mechanism of ZnO absorption into the *Nata de sago* bacterial cellulose matrix is thought to occur through Van der Waals interactions between the ZnO-purified mangosteen peel extract from the ethyl acetate-methanol fraction and hydroxyl oxygen atoms in the *Nata de sago* bacterial cellulose [42], [43]. The proposed interaction of bacterial cellulose with the ZnO-purified mangosteen peel extract from the ethyl acetate-methanol fraction is shown in Figure 19. This interaction causes ZnO to be trapped in the pores of the *Nata de sago* bacterial cellulose. The trapped ZnO has plasmonic properties that allow this transparent film to increase the sensitivity of Cr (VI) metal detection by UV-Vis spectrophotometry.

The detection mechanism occurs through the formation of a coordinate covalent bond between Cr(VI) and an electron pair donor ligand in the cellulose functional group (hydroxyl ligand) which weakens the coordinate covalent bond between cellulose and ZnO. This weakening causes a decrease in the size of the ZnO nanoparticles which is directly proportional to the concentration of Cr(VI). Qualitatively, changes in the size of ZnO are confirmed by changes in colour and SPR wavelength of Cr(VI) measurements with different concentrations.

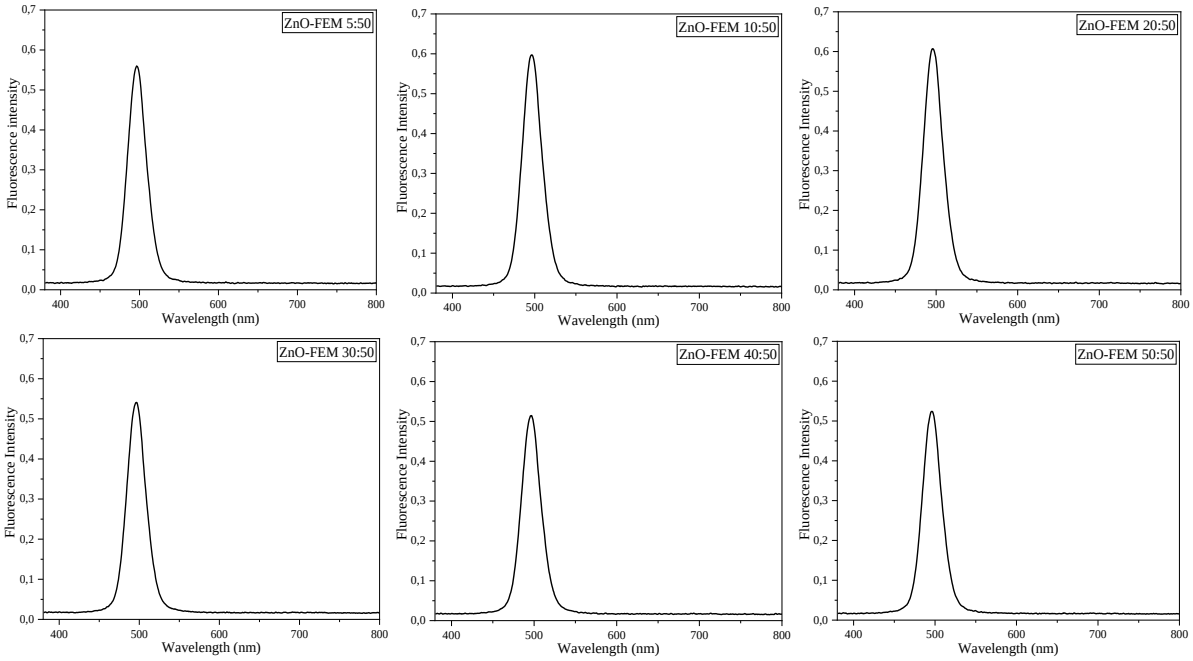

Figure 20. Fluorescence of ZnO.

Optical Properties

The optical properties of ZnO nanomaterials play an important role in determining their performance in various applications, especially in optical sensors and devices. In this study, ZnO powder was dispersed in 96 % ethanol to study its optical characteristics by measuring the fluorescence spectrum and band gap values. Figure 20 shows the fluorescence of ZnO at an excitation wavelength of 500 nm. The fluorescence intensity of ZnO was varied. In the ZnO-FEM 5:50 and ZnO-FEM 10:50 samples, the fluorescence intensity was low, but it increased at the ZnO-FEM ratio of 20:50, and decreased significantly with ZnO-FEM 30:50, ZnO-FEM 40:50, and ZnO-FEM 50:50. These changes were likely influenced by the concentration and density factors of ZnO in the solvent. If the concentration or density is too high, it may increase the fluorescence intensity, while if it is too low, the resulting fluorescence intensity may also be weaker.

The band gap value of ZnO thin films was determined through optical absorption spectrum analysis. The band gap value was calculated using the equation:

$$(\alpha hv) = A(hv - E_g)^{1/2}$$

where α is the absorption coefficient, h is Planck's constant, v is the frequency of the incident radiation, and E_g is the band gap energy. A graph of $(\alpha hv)^2$ against hv was plotted, and the band gap value was obtained by extrapolating the straight-line portion to hv (α = 0) [44]. The band gap energy graphs of ZnO can be seen in Figure 21.

These results indicate that ZnO-FEM 5:50, ZnO-FEM 10:50, ZnO-FEM 20:50, ZnO-FEM 30:50, ZnO-FEM 40:50, and ZnO-FEM 50:50 had band gap energy values of 1.985 eV, 2.060 eV, 1.926 eV, 1.966 eV, 2.036 eV, and 2.17 eV, respectively. Optically, the band gap values indicate that ZnO has semiconductor properties with allowed direct transitions [45]. This means that ZnO can efficiently absorb light with energy greater than its band gap, such as ultraviolet light, but remains transparent in the visible light region. This property makes ZnO suitable for optical sensor applications, thanks to its good absorption ability in a certain energy range.

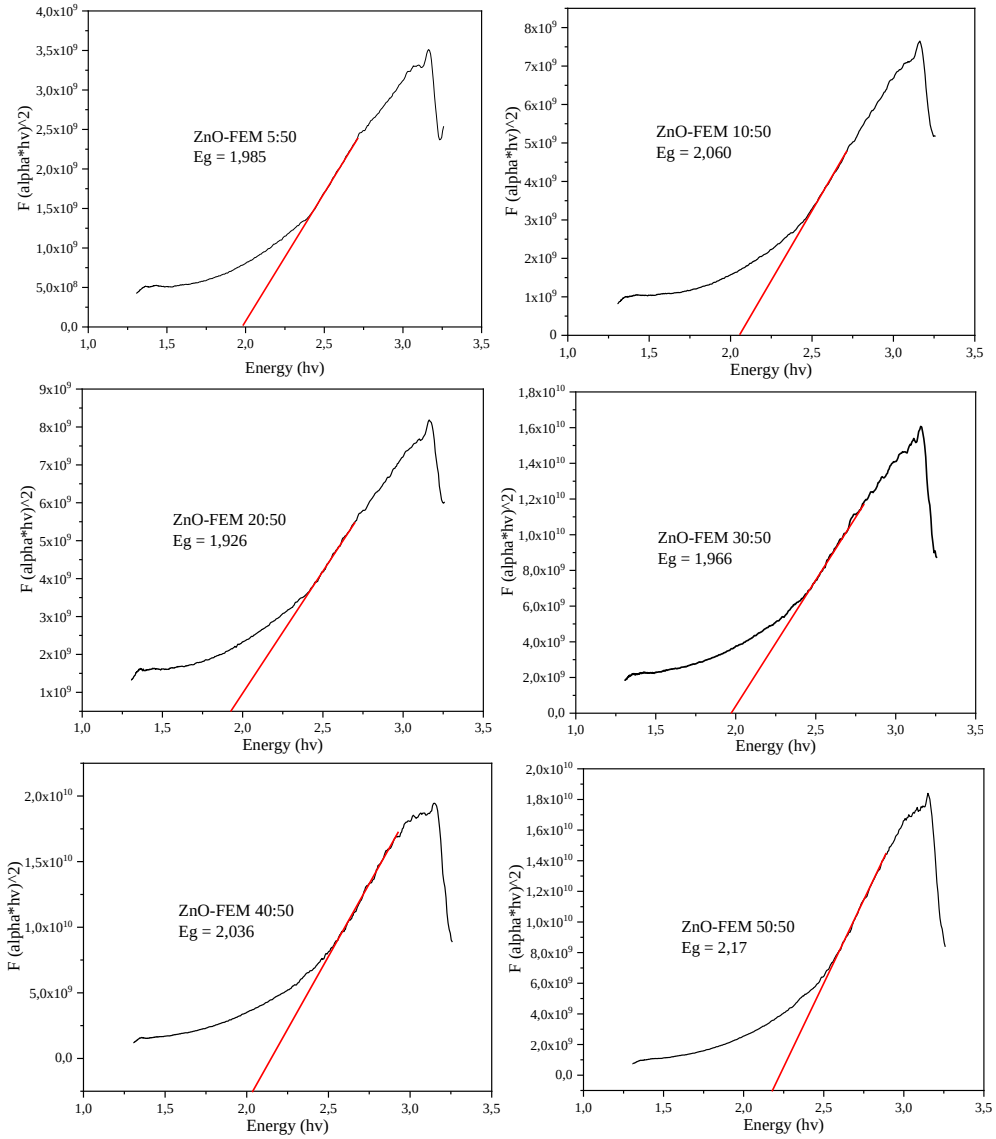

Figure 21. Band Gap Energies of ZnO

Film Test

The film test started with a preliminary test to obtain the coefficient of determination (R^2) value for each transparent film of *Nata de sago* bacterial cellulose incorporated with the ZnO-FEM nanostructure (abbreviated as NBC-ZnO-FEM). The NBC-ZnO-FEM transparent film was tested using standard Cr(VI) solutions of 0.01, 0.10, 0.20, 0.40, 0.60, 0.80, and 1.00 ppm by UV-Vis spectrophotometry. The absorbance data obtained were plotted against the standard Cr(VI) concentration as a calibration curve. The calibration curves obtained are shown in Figure 22.

The calibration curves all showed a linear relationship between Cr(VI) concentration and absorbance. The higher the concentration, the higher the absorbance. The best R^2 value (0.9996) was found using the NBC-ZnO-FEM 40:50 transparent film. The calibration curve was acceptable because the R^2 values obtained was very close to 1 [46]. Therefore, the validity of the Cr(VI) measurement method by UV-Vis spectrophotometry using this transparent film was determined based on the sensitivity, accuracy, precision, LOD, and LOQ values developed from the measurement data included in this calibration curve.

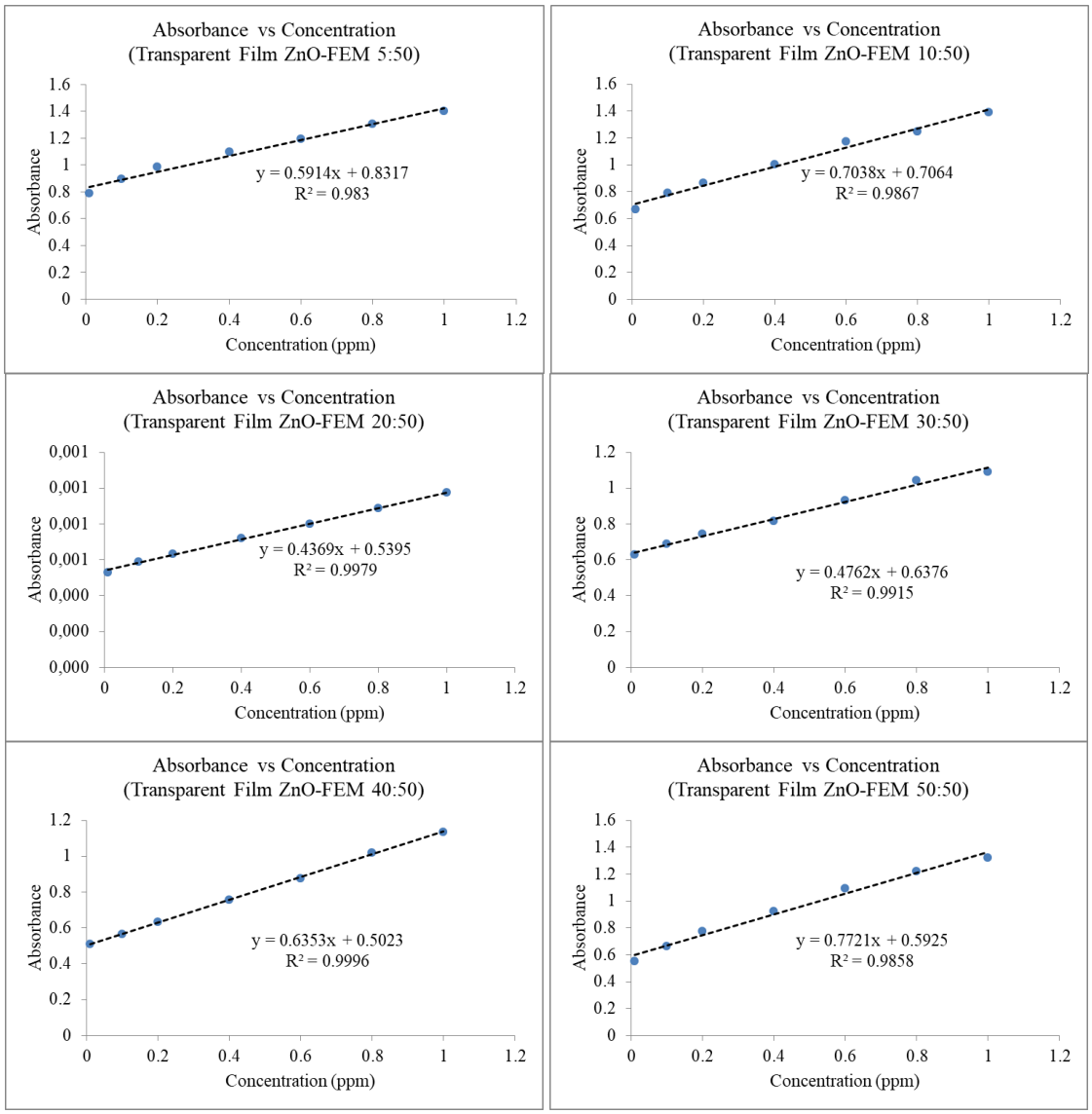

Figure 22. Calibration curves of transparent films of *Nata de sago* bacterial cellulose incorporated with ZnO-FEM nanostructures in standard solutions of Cr(VI).

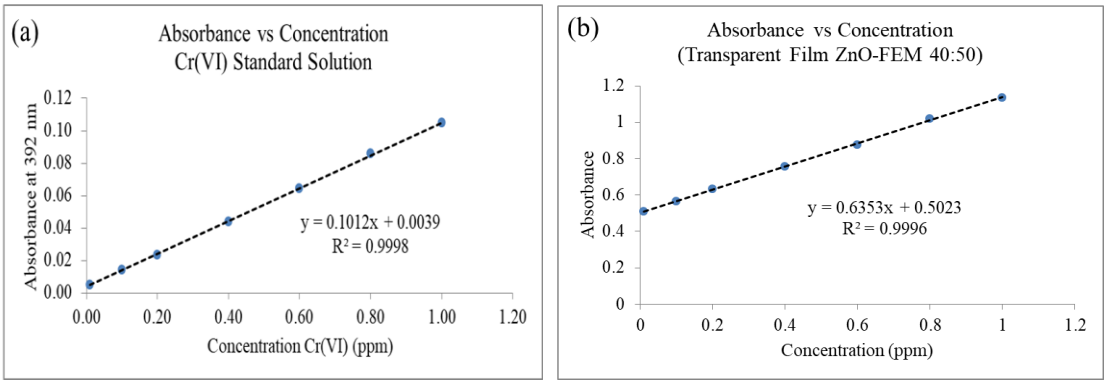

Figure 23. Calibration curves of UV-Vis spectrophotometric measurements of Cr(VI) standard solution (a) using without the film, (b) using a transparent film of *Nata de sago* bacterial cellulose incorporated with ZnO-FEM 40:50.

Method Validation

Method validation is an important aspect to ensure that an analytical technique provides accurate, consistent results and is in accordance with the purpose of the test. The first validity parameter is sensitivity. Sensitivity was calculated based on the slope value obtained from the calibration curve of the measurement of the Cr(VI) standard solution using a transparent film of NBC-ZnO-FEM 40:50, and compared with the slope value of the measurement without using the film by UV-Vis spectrophotometry. Determination of sensitivity was carried out through analysis of the linear regression equation value on the standard curve with the equation $y = ax + b$, where the slope value a represents the level of sensitivity of the method. A higher slope value indicates that the method has a better ability to detect small changes in Cr(VI) concentration. The calibration curves of the UV-Vis spectrophotometric measurements of the Cr(VI) standard solution with and without a transparent film of NBC-ZnO-FEM 40:50 can be seen in Figure 23.

Based on the linear regression equation values with the transparent film NBC-ZnO-FEM 40:50 and without the film, the slope values of 0.6353 and 0.1012 were obtained, respectively. This shows that measurements using the transparent film NBC-ZnO-FEM 40:50 had good sensitivity compared to measurements without the transparent film.

In addition to sensitivity, accuracy and precision are also important parameters in the validation of the method. Accuracy measures how close the analysis results are to the actual analyte levels. Accuracy is expressed in the form of percentage recovery (% recovery) and can be determined using the standard addition method. The addition of a standard solution, or spike, was done by adding a 0.01 ppm solution of Cr(VI) to a nickel smelter wastewater sample, to evaluate the accuracy of the analysis method. By adding a spike, the % recovery of the added analyte can be calculated accurately.

Precision refers to the degree of closeness of the measurement results in a series of analyses performed on the same sample. Precision indicates how consistent the results are when the analysis is repeated under the same conditions. Measurement precision refers to the percentage value of the relative standard deviation (%RSD). Data for determining % recovery and % RSD are presented in Table 3. The results of this study indicate that % recovery was in the range of 80 – 110 %, so it can be said that the measurement of Cr(VI) metal using this method had good accuracy. The %RSD value obtained indicates that the measurement precision met the validation criteria, as reported from previous research results [47].

Another validation parameter is the limit of detection (LOD) which is defined as the smallest amount of analyte in a sample that can still be detected by a measuring instrument without the need for quantitation. The limit of quantitation (LOQ) is the lowest concentration limit of the analyte in a sample that meets the precision and accuracy criteria. The results of the LOD and LOQ calculations using a standard solution of Cr(VI) 0.01 ppm are presented in Table 3. By entering the LOD absorbance of 0.51108 and the LOQ absorbance of 0.51427 (y value) into the regression equation of the calibration curve of the transparent film of *Nata de sago* bacterial cellulose incorporated with ZnO-FEM 40:50 nanostructure, the LOD and LOQ concentrations (x value) obtained were 0.0138 ppm and 0.0188 ppm, respectively.

Table 3. Method validation results.

Repetition	Absorbance Cr(VI) Standard Solution 0.01 ppm	Absorbance of Real Sample + Spike Cr(VI) 0.01 ppm
1	0.5108	0.52066
2	0.5101	0.52114
3	0.5101	0.52180
4	0.5084	0.52049
5	0.5109	0.52130
6	0.5090	0.52149
7	0.5087	0.52103
Average	0.5097	0.52113
SD	0.00045	
%Recovery		102%
%RSD	0.09%	
LOD = $X_{average}$ + 3 SD	0.51108 Absorbance	0.0138 ppm
LOQ = $X_{average}$ + 10 SD	0.51427 Absorbance	0.0188 ppm

Plotting the absorbance value of the nickel smelter liquid waste sample solution on the calibration curve of the standard solution using a transparent film of NBC-ZnO-FEM 40:50 produced a Cr(VI) concentration value of 0.01843 ppm in the measured sample. This study showed a high sensitivity for detecting Cr(VI), with a detection limit of 0.0138 ppm and the best R^2 value of 0.9996, making it more sensitive in detecting Cr(VI) compared to the previous method developed by Firdaus et al. (2023) on the detection of Cr(VI) using gold nanoparticles (AuNPs) by UV-Vis spectrophotometry [48].

CONCLUSION

Transparent films made from *Nata de Sago* bacterial cellulose were successfully developed by incorporating ZnO nanostructures synthesized using purified mangosteen peel extract as a green capping agent. The ethyl acetate-methanol fraction of this extract played an important role in controlling the morphology of ZnO, resulting in highly stable and evenly distributed nanoparticles with optimal optical and structural properties. The smallest crystallite size achieved was 8.91 nm, as confirmed by XRD analysis.

The transparent film of *Nata de sago* bacteria cellulose incorporated with ZnO-FEM 40:50 showed excellent performance in the detection of Cr(VI) by UV-Vis spectrophotometry, with a sensitivity of 0.6353, LOD of 0.0138 ppm, LOQ of 0.0188 ppm, precision (%RSD) of 0.09 %, and accuracy (% recovery) of 102 %. This film offered a reliable, environmentally friendly, and efficient solution for the detection of Cr(VI), thus having good potential as a photometric sensor for monitoring heavy metal ions in aquatic environments.

It must be noted that this study had several limitations, e.g., it focused on detecting only Cr(VI), tests were performed in a controlled laboratory environment, and the long-term stability of the film under extreme conditions had not been evaluated. Therefore, further studies are needed to assess the film's capability in detecting other heavy metal ions, such as Cd and Hg, as well as in-situ testing to validate its performance. Additionally, the development of plasmonic films with other metal oxides and the integration of machine learning for data analysis could represent promising future research directions to enhance the effectiveness, resolution, and applications of this sensor.

ACKNOWLEDGEMENTS

The authors extend their gratitude to the Ministry of Education, Culture, Research and Technology, Republic of Indonesia, particularly to the Directorate of Research and Community Service for the research grant as per the Research Program Implementation Contract Number: 049/E5/PG.02.00.PL/2024 dated 11 June 2024, and acknowledge the Institute for Research and Community Service, Halu Oleo University.

REFERENCES

1. Sharma, P., Singh, S. P., Parakh, S. K. and Tong, Y. W. (2022) Health hazards of hexavalent chromium (Cr (VI)) and its microbial reduction. *Bioengineered*, **3**, 4923–4938.

2. Shraim, A. M., Ahmad, M. I., Rahman, M. S. F. and Ng, J. C. (2022) Concentrations of essential and toxic elements and health risk assessment in brown rice from Qatari market. *Food Chemistry*, **376**, 131938.

3. Santarcangelo, C., Baldi, A., Ciampaglia, R., Dacrema, M., Di Minno, A., Pizzamiglio, V., Tenore, G. C., Daglia, M. (2022) Long-aged parmigiano reggiano PDO: Trace element determination targeted to health. *Foods*, **11**, 1–11.

4. Dai, L., Wang, Y., Zou, X., Chen, Z., Liu, H. and Ni, Y. (2020) Ultrasensitive physical, Bio, and chemical sensors derived from 1-, 2-, and 3-D nanocellulosic materials. *Small*, **16**, 1–25.

5. Nurhidayah, N., Ramadhan, L. O. A. N., Watoni, A. H., Kadir, L. A., Rahmatullah, M. D. and Haruna, C. A. (2024) Bacterial cellulose incorporated zinc phosphate nanocomposite for antibacterial agent and air particulate matter filtration. *Malaysian Journal of Science*, **43**, 22–33.

6. Silviana, S., Santo Khoirudin, F., Pratama, F. A., Harahap, R. P. A., Hasanah, A., Ruhmaningrum, Q. and Salsabila, C. A. (2022) Non-Microplastic microbeads from sago liquid waste with the addition of chitosan as antibacterial function: A Review. *Teknik*, **43**, 211–221.

7. Mei, G. S., Menon, P. S., and Hegde, G. (2020) ZnO for performance enhancement of surface plasmon resonance biosensor: a review. *Materials Research Express*, **7**, 1–17.

8. Tereshchenko, A., Bechelany, M., Viter, R., Khranovskyy, V., Smyntyna, V., Starodub, N. and Yakimova, R. (2016) Optical biosensors based on ZnO nanostructures: advantages and perspectives. A review. *Sensors and Actuators B: Chemical*, **229**, 664–677.

9. Obolskiy, D., Pischel, I., Siriwatanametanon, N. and Heinrich, M. (2009) Garcinia mangostana L.: a phytochemical and pharmacological review. *Phytotherapy Research: An International Journal Devoted to Pharmacological and Toxicological Evaluation of Natural Product Derivatives*, **23**, 1047–1065.

10. Kołodziejczak-Radzimska, A., Jesionowski, T. and Krysztafkiewicz, A. (2010) Obtaining zinc oxide from aqueous solutions of KOH and Zn(CH3COO)2. *Physicochemical Problems of Mineral Processing*, **44**, 93–102.

11. Jia, W., Dang, S., Liu, H., Zhang, Z., Yu, C., Liu, X. and Xu, B. (2012) Evidence of the formation mechanism of ZnO in aqueous solution. *Materials Letters*, **82**, 99–101.

12. Kumar, K. M., Mandal, B. K., Naidu, E. A., Sinha, M., Kumar, K. S. and Reddy, P. S. (2013) Synthesis and characterisation of flower shaped zinc oxide nanostructures and its antimicrobial activity. *Spectrochimica Acta Part A: Molecular and Biomolecular Spectroscopy*, **104**, 171–174.

13. Mahato, T. H., Prasad, G. K., Singh, B., Acharya, J., Srivastava, A. R. and Vijayaraghavan, R. (2009) Nanocrystalline zinc oxide for the decontamination of sarin. *Journal of Hazardous Materials*, **165**, 928–932.

14. Ismail, A. A., El-Midany, A., Abdel-Aal, E. A. and El-Shall, H. J. M. L. (2005) Application of statistical design to optimize the preparation of ZnO nanoparticles via hydrothermal technique. *Materials Letters*, **59**, 1924–1928.

15. Dem'Yanets, L. N., Li, L. E. and Uvarova, T. G. (2006) Zinc oxide: hydrothermal growth of nano-and bulk crystals and their luminescent properties. *Journal of Materials Science*, **41**, 1439–1444.

16. Kołodziejczak-Radzimska, A., Markiewicz, E. and Jesionowski, T. (2012) Structural characterisation of ZnO particles obtained by the emulsion precipitation method. *Journal of Nanomaterials*, **2012**, 656353.

17. Chen, D., Jiao, X. and Cheng, G. (1999) Hydrothermal synthesis of zinc oxide powders with different morphologies. *Solid State Communications*, **113**, 363–366.

18. Li, P., Wei, Y., Liu, H. and Wang, X. K. (2005) Growth of well-defined ZnO microparticles with additives from aqueous solution. *Journal of Solid State Chemistry*, **178**, 855–860.

19. Li, X., He, G., Xiao, G., Liu, H. and Wang, M. (2009) Synthesis and morphology control of ZnO nanostructures in microemulsions. *Journal of Colloid and Interface Science*, **333**, 465–473.

20. Vorobyova, S. A., Lesnikovich, A. I. and Mushinskii, V. V. (2004) Interphase synthesis and characterization of zinc oxide. *Materials Letters*, **58**, 863–866.

21. Yuvakkumar, R., Suresh, J., Nathanael, A. J., Sundrarajan, M. and Hong, S. I. (2014) Novel green synthetic strategy to prepare ZnO nanocrystals using rambutan (Nephelium lappaceum L.) peel extract and its antibacterial applications. *Materials Science and Engineering: C*, **41**, 17–27.

22. Marfu'ah, S., Rohma, S. M., Fanani, F., Hidayati, E. N., Nitasari, D. W., Primadi, T. R., Ciptawati, E., Sumari, S. and Fajaroh, F. (2020) Green synthesis of ZnO nanoparticles by using banana peel extract as capping agent and its bacterial activity. In IOP Conference Series: *Materials Science and Engineering*, **833**, 1–6.

23. Abomuti, M. A., Danish, E. Y., Firoz, A., Hasan, N. and Malik, M. A. (2021) Green synthesis of zinc oxide nanoparticles using salvia officinalis leaf extract and their photocatalytic and antifungal activities. *Biology*, **10**, 1–26.

24. Klinbumrung, A., Panya, R., Pung-Ngama, A., Nasomjai, P., Saowalakmeka, J. and Sirirak, R. (2022) Green synthesis of ZnO nanoparticles by pineapple peel extract from various alkali sources. *Journal of Asian Ceramic Societies*, **10**, 755–765.

25. Shabaani, M., Rahaiee, S., Zare, M. and Jafari, S. M. (2020) Green synthesis of ZnO nanoparticles using loquat seed extract; Biological functions and photocatalytic degradation properties. *LWT - Food Science and Technology*, **134**, 1–10.

26. Uysal, Y., Görkem Doğaroğlu, Z., Çaylali, Z. and Karakulak, D. S. (2024) Rosemary-Mediated Green Synthesis of ZnO Nanoparticles and their Integration into Hydrogel Matrices: Evaluating Effects on Wheat Growth and Antibacterial Properties. *Global Challenges*, **2400120**, 1–17.

27. Fadhila, N. A., Sriwidodo, S., Chaerunisaa, A. Y. (2022) Instant Granules of Mangosteen Peel (Garcinia Mangostana L.) Ethanol Extract as Antioxidants. *Sciences of Pharmacy*, **1**, 1–6.

28. Zhu, F., Zhao, B., Hu, B., Zhang, Y., Xue, B., Wang, H. & Chen, Q. (2023) Review of available "extraction+ purification" methods of natural ceramides and their feasibility for sewage sludge analysis. *Environmental Science and Pollution Research*, **30**, 68022–68053.

29. Keskes, H., Belhadj, S., Jlail, L., El Feki, A., Damak, M., Sayadi, S. & Allouche, N. (2017) LC-MS–MS and GC-MS analyses of biologically active extracts and fractions from Tunisian Juniperus phoenice leaves. *Pharmaceutical Biology*, **55**, 88–95.

30. Yanti, N. A., Ambardini, S., Walhidayah, T., Ahmad, S. W., Ramadhan, L. O. A. N., Santi, M.,

Indrawati, and Muhsin (2023) Application of antibacterial and antioxidant edible coating incorporating bacterial cellulose from sago liquid waste and garlic for preservation of tomato (Solanum lycopersicum L.). *International Food Research Journal*, **30**, 1330–1340.

31. Sun, Y., Zhang, W., Li, Q., Liu, H. and Wang, X. (2023) Preparations and applications of zinc oxide based photocatalytic materials. *Advanced Sensor and Energy Materials*, **100069**, 1–19.

32. Al Rahbi, A. S., Al Mawali, A. H., Al Rawahi, S. S., Al Dighishi, R. K., Al Abri, F. A., Ahmed, A. and Rahman, S. (2024) Green synthesis of zinc oxide nanoparticles from Salvadora persica leaf extract: Characterization and studying methyl orange removal by adsorption. *Water Practice & Technology*, **19**, 1219–1231.

33. Suciyati, S. W., Manurung, P., Junaidi, J. and Situmeang, R. (2024) Optical and Crystal Structure Properties of ZnO Nanoparticle Synthesized through Biosynthesis Method for Photocatalysis Application. *Indonesian Journal of Chemistry*, **24**, 125–140.

34. Wahab, R., Ansari, S. G., Kim, Y. S., Dar, M. A. and Shin, H. S. (2008) Synthesis and characterization of hydrozincite and its conversion into zinc oxide nanoparticles. *Journal of Alloys and Compounds*, **461**, 66–71.

35. Elumalai, K. and Velmurugan, S. (2015) Green synthesis, characterization and antimicrobial activities of zinc oxide nanoparticles from the leaf extract of Azadirachta indica (L.). *Applied Surface Science*, **345**, 329–336.

36. Hameed, H., Waheed, A., Sharif, M. S., Saleem, M., Afreen, A., Tariq, M., Kamal, A., Al-onazi, W. A., Al Farraj, D. A., Ahmad, S. and Mahmoud, R. M. (2023) Green synthesis of zinc oxide (ZnO) nanoparticles from green algae and their assessment in various biological applications. *Micromachines*, **14**, 928.

37. Seydioglu, T., Kurnaz, S., Tokeşer, E. A., Yildirim, G. and Ozturk, O. (2024) Effect of foreign impurity and growth temperatures on hexagonal structure and fundamental properties of ZnO nanorods. *Microscopy Research and Technique*, **2024**, 1–14.

38. Mustapha, S., Ndamitso, M. M., Abdulkareem, A. S., Tijani, J. O., Shuaib, D. T., Mohammed, A. K. and Sumaila, A. (2019) Comparative study of crystallite size using Williamson-Hall and Debye-Scherrer plots for ZnO nanoparticles. *Advances in Natural Sciences: Nanoscience and Nanotechnology*, **10**, 045013.

39. Ismail, M. A., Taha, K. K., Modwi, A. and Khezami, L. (2018) ZnO nanoparticles: Surface and X-ray profile analysis. *J. Ovonic Res*., **14**, 381–393.

40. Soto-Robles, C. A., Luque, P. A., Gómez-Gutiérrez, C. M., Nava, O., Vilchis-Nestor, A. R., Lugo-Medina, E., Ranjithkumar and Castro-Beltrán, A. (2019) Study on the effect of the concentration of Hibiscus sabdariffa extract on the green synthesis of ZnO nanoparticles. *Results in Physics*, **15**, 1–8.

41. Sarifudin, Ramadhan, A. and Mardin, S. (2024) Development of an entrepreneurship teaching module based on research on the use of white langquas (Alpinia galanga) on the quality of nata de coco. *International Journal of Science and Research Archive*, **12**, 1022–1031.

42. Williams, S., Okolie, C. L., Deshmukh, J., Hawco, L., McNeil, J., Nganou Assonkeng, A. C., Bennett and Mkandawire, M. (2019) Magnetizing cellulose fibers with CoFe2O4 nanoparticles for smart wound dressing for healing monitoring capability. *ACS Applied Bio Materials*, **2**, 5653–5662.

43. Watoni, A. H., Ramadhan, L. O. A. N., Adha, E. N. and Sudarman, R. (2023) The study of plasmonic chip of nata de sago-green silver nanoparticles for detection of blood glucose. *Chimica et Natura Acta*, **11**, 59–69.

44. Jamil, M. T., Ahmad, J., Bukhari, S. H., Sultan, T., Akhter, M. Y., Ahmad, H. and Murtaza, G. (2017) Effect on structural and optical properties of Zn-substituted cobalt ferrite CoFe2O4. *Journal of Ovonic Research*, **13**, 45–53.

45. Amakali, T., Daniel, L. S., Uahengo, V., Dzade, N. Y. and De Leeuw, N. H. (2020) Structural and optical properties of ZnO thin films prepared by molecular precursor and sol–gel methods. *Crystals*, **10**, 1–11.

46. Mukaka, M. M. (2012) Statistics Corner: A Guide to Appropriate Use of Correlation Coefficient in Medical Research. *Malawi Medical Journal*, **24**, 69–71.

47. Adu, J. K., Amengor, C. D., Orman, E., Ibrahim, N. M., Ifunanya, M. O. and Arthur, D. F. (2019) Development and Validation of UV-Visible Spectrophotometric Method for the Determination of 5-Hydroxymethyl Furfural Content in Canned Malt Drinks and Fruit Juices in Ghana. *Journal of Food Quality*, **2019**, 1–8.

48. Firdaus, M. L., Apriyoanda, H., Isnan, I., Wyantuti, S. and Eddy, D. R. (2023) Quantitative analysis of Cr (III) and Cr (VI) using gold nanoparticles with UV-vis spectrometry and smartphone colorimetric-sensing. *Iran. J. Chem. Chem. Eng. Research Article*, **42**, 1–9.